IEEE Access
Multidisciplinary | Rapid Review | Open Access Journal

Received February 6, 2020, accepted March 4, 2020, date of publication March 13, 2020, date of current version March 25, 2020.

Digital Object Identifier 10.1109/ACCESS.2020.2980595

Research on Structurally Integrated Phased Array for Wireless Communications

QING-QIANG HE[1], SHUAI DING[2], CHEN XING[1], JUN-QUAN CHEN[1], GUO-QING YANG[1], AND BING-ZHONG WANG[2], (Senior Member, IEEE)

[1]Southwest China Institute of Electronic Technology, Chengdu 610036, China
[2]Institute of Applied Physics, University of Electronic Science and Technology of China, Chengdu 610054, China

Corresponding authors: Qing-Qiang He (heqingqiang518@126.com) and Shuai Ding (uestcding@uestc.edu.cn)

This work was supported in part by the National Natural Science Foundation of China under Grant 61601087, in part by the Fundamental Research Funds for the Central Universities under Grant ZYGX2019Z016, and in part by the Sichuan Science and Technology Program under Grant 2018GZ0518 and Grant 2019YFG0510.

ABSTRACT Structurally integrated antenna is a kind of highly integrated microwave device with a load-bearing function, and it is usually installed on the structural surface of the air, water and ground vehicles. This paper presents the design, fabrication and testing of a novel structurally integrated Ka-band active antenna for airborne 5G wireless communications. The proposed antenna is mainly composed of three parts: a package layer, a control and signal process layer and a RF layer. In the RF layer, the microstrip antenna array, tile transmitting (Tx) modules, micro-channel heat sinks and a stripline feeding network are highly integrated into a functional block with a thickness of 2.8 mm. Electromechanical co-design methods are developed to design the active antenna array with the superstrates, and two schemes for designing micro-channel heat sinks are evaluated to obtain a uniform temperature distribution. The RF layer is fabricated by using the low-temperature cofired ceramic process, and the three layers are assembled to form the full-size antenna prototype. The mechanical and electromagnetic experiments are carried out, and the results demonstrate the feasibility of the structurally integrated active antenna for airborne wireless communications.

INDEX TERMS 5G communications, phased array antenna, structurally integrated active antenna, low-temperature cofired ceramic (LTCC), micro-channel heat sinks.

I. INTRODUCTION

Significant momentum has started to build around the 5G wireless communication technologies for delivering mobile experience differentiation by providing higher data rates, lower latency, and improved link robustness [1], [2]. In this regard, millimeter-wave phased array antenna is a very promising solution for 5G wireless communications, due to the wide bandwidths and steerable beams. The millimeter-wave phased array antenna can be applied to realize the wireless connection between the base stations and wireless terminals in a mobile vehicle such as the aircraft, high-speed train, car, and ship. Moreover, it can be continuously steered to the base stations, which could guarantee reliable connections in these mobile environments [3]–[5]. In addition, the multi-gigabits-per-second data speeds in 5G will provide new wireless communication applications such as uncompressed video streaming, mobile distributed computing, fast large file transfer, and office in a high-speed mobile environment [6]. However, because of the limited space in a mobile vehicle like the aircraft, the phased array antenna is usually required to have a compact size, light weight and easy installation [7]. In this condition, it is highly desirable to use structurally integrated active antennas for 5G wireless communications in a mobile vehicle.

Structurally integrated active antennas can embed an active planar printed antenna into the structural surface of the aircraft, high-speed train, car, ship, and armored vehicles [8]–[11]. For example, the active microstrip antenna array is integrated into the wing or fuselage of an aircraft. Compared with the antennas mounted on the structural surface, structurally integrated active antenna features several advantages such as reduced weight, volume and aerodynamic drag. Structurally integrated active antenna is a kind of highly integrated antenna, which receives great attention in recent years. Antenna-on-chip (AoC) and antenna-in package (AiP) solutions are two commonly used techniques to realize the highly integrated antennas [12]–[14]. Compared to AiP, AoC

The associate editor coordinating the review of this manuscript and approving it for publication was Yasar Amin.

solutions eliminate the need of off-chip connections between dies and antennas, but reduce the reliability on manufacturing precision [15]. Low-temperature cofired ceramics (LTCC) and liquid crystal polymer (LCP) are two very attractive materials for fabricating the AiP [12], and the mainstream SiGe or CMOS technologies are usually adopted to fabricate the AoC [12], [15], [16]. In [17], the authors conducted a chronological review of the research on the AiPs using the LTCC, and the AiPs applied to realize the millimeter-wave communication were demonstrated in [18]–[25]. LCP is also a competitive substrate and packaging material due to its excellent electrical properties, flexibility, and multi-layer lamination capability. Several researchers have utilized the LCP to fabricate the AiP and demonstrated wideband, high-gain, and high-efficiency antenna applications [26]–[29]. All of the studies promote the development of highly integrated antennas. However, most of the previous studies concentrate on the antenna technology, interconnect and package processes, while the heat dissipation of the highly integrated active antennas is not considered. Besides, the AiP and AoC cannot be directly installed on the structural surface of the aircraft, high-speed train, car, ship, and armored vehicles, due to the lack of the load-bearing function. Different from the AiP and AoC, this work proposes a structurally integrated active antenna which can simultaneously provide a load-bearing skin and a receiving or sending electromagnetic microwave device.

Nowadays, the antennas with a load-bearing function are also of great interest in antenna fields. Researchers have proposed different concepts, such as conformal load-bearing antennas [30]–[32], smart skin antenna [33], three-dimensionally integrated microstrip antenna [34], composite antenna array [35], and so on. The basic configuration of the antenna array shown in Fig. 1 is a sandwich construction consisting of facesheet, honeycomb core, microstrip or planar spiral antenna and feeding networks. The antennas and feeding networks are inserted into the facesheet and honeycomb, and the epoxy adhesive is applied to bond the different components and form the final antenna with the load-bearing function. From the reported literature, it is found that almost all of the investigations are dedicated to the design and fabrication of the structurally integrated passive antenna [36]–[40]. However, in practice, the structurally integrated active antenna is usually required for future 5G wireless communications, due to its steerable beam pointing capability.

This work focuses on the design, fabrication and experiments of a novel structurally integrated active antenna. The motivation of this investigation is to develop an active skin antenna for realizing the 5G wireless communication between the aircraft and the base stations.

Compared with the existing work, the proposed highly integrated antenna consists of a package layer, a control and signal process layer and a RF layer, and can provide a load-bearing function and a steerable beam pointing capability simultaneously. Electromechanical co-design methods are applied to design the antenna array with the superstrates,

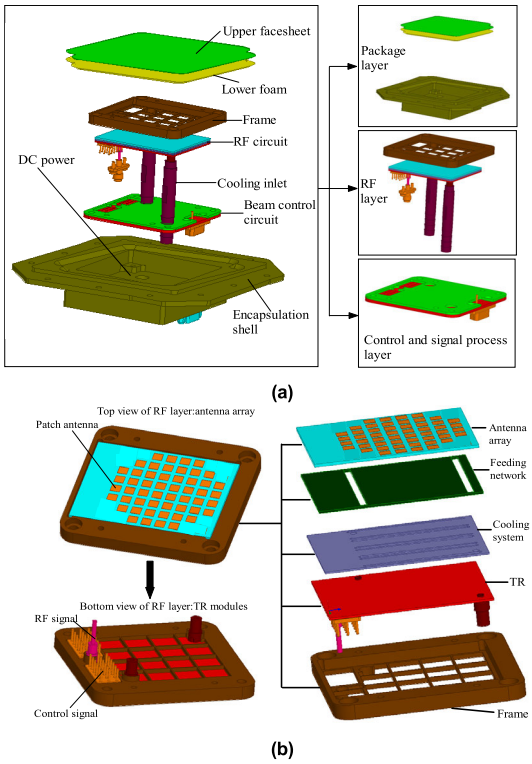

FIGURE 1. Schematic diagram of structurally integrated phased array. (a) Overall structural configuration. (b) Exploded view of the RF layer structure.

and two design schemes for the micro-channel heat sinks are investigated and compared to obtain a uniform temperature distribution. The LTCC technology is applied to fabricate the RF layer, where the antenna array, Tx modules, micro-channel heat sinks and feeding network are integrated into a functional block with a thickness of 2.8 mm. The mechanical load-bearing and electromagnetic performance are measured, and the results demonstrate the feasibility of the structurally integrated active antenna prototype.

The rest of the work is organized as follows. Sec. II presents the design of the structurally integrated active antenna, and Sec. III succinctly describes the fabrication of the antenna prototype. In addition, Sec. IV presents the mechanical and electromagnetic experimental results, while Sec. IV discusses the impact of the mechanical structure on the performance of the array. Finally, a short conclusion is drawn in Sec. VI.

II. DESIGN OF STRUCTURALLY INTEGRATED PHASED ARRAY

A. SCHEMATIC

Figure 1 shows the schematic diagram of the antenna array system. The system consists of a package layer, a RF layer and a processing layer. The package layer includes the DC voltage source which supplies the power required by the phased array, and can simultaneity achieve impact and environmental resistances. The RF layer provides the receiving

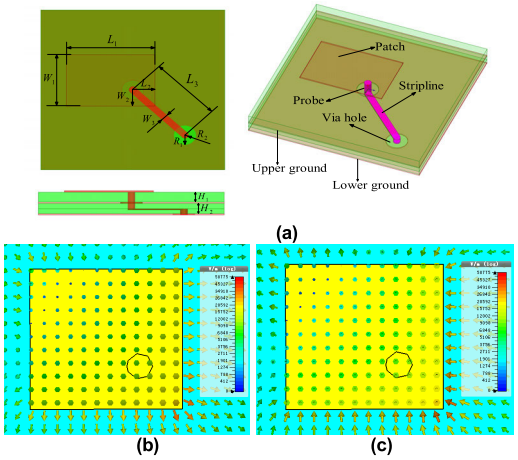

FIGURE 2. The proposed microstrip antenna element- dimension parameters and prospective view. (a) structure (b) E-field (phase=0) (c) E-field (phase=180°) FIGURE 3. VSWR and axial ratio of the antenna element.

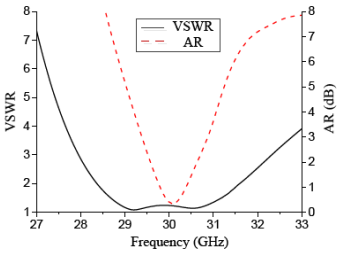

FIGURE 3. VSWR and axial ratio of the antenna element.

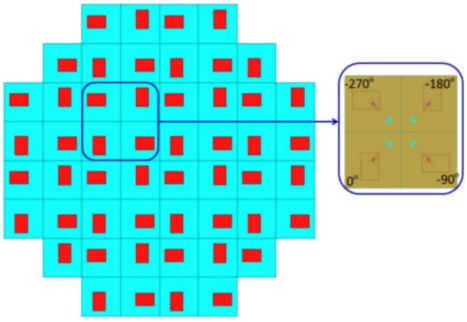

FIGURE 4. Layout of the antenna array-overall array and 2 × 2 sub-array.

and transmitting function in the RF regime, which consists of a micro-strip antenna array, tile-style TR modules, a micro-channel cooling system and a strip-line feeding network. The processing layer comprises mainly the beam control circuit and the processing chip which generates the controlling signal to realize beam scanning.

Figure 1(b) shows the exploded view of the RF layer structure. It is fabricated by the LTCC technology. The micro-channel cooling system is located between the feeding network and TR modules. The TR modules are integrated on the rear side of the cooling system. All elements in the antenna array are connected to the TR modules through the perpendicular interconnects. In order to improve the structural stiffness and strength, the aluminum is used to fabricate the frame and encapsulate shell. The radome on the package layer is made up of upper facesheet and lower foam. The lower foam between the upper facesheet and the antenna array is bonded by the epoxy adhesive to form the antenna prototype.

B. DESIGN OF ACTIVE ANTENNA ARRAY WITH SUPERSTRATES

The active antenna array in the RF layer is protected by the super-strates which consist of the upper facesheet and the lower foam. In this subsection, we present the design procedure of the active antenna array with the super-strates. The first step is to design the antenna array without the super-strates. Figure 2 shows the geometry of a single microstrip antenna element. It was designed using the Ferro A6M LTCC tape, with a relative dielectric constant of 5.9 and a loss tangent of 0.002. The thickness of each LTCC layer is 0.1 mm. The rectangular patch is fed at the diagonal by a vertical probe to excite two orthogonal modes for circularly polarized radiation. The feeding probe is connected to a stripline through via hole of the ground plane. To enhance the impedance matching, ground vias are employed around the feeding probe and the end of the stripline. Besides, the substrate for the radiating patch is 0.5 mm thick (5 LTCC layers), and the distance between the upper and lower ground planes is 0.2 mm (2 LTCC layers). The detailed dimensions of the optimized parameters in Fig. 2 are as follows (unit: mm): $W_1 = 1.63$, $W_2 = 0.5$, $W_3 = 0.25$, $L_1 = 1.78$, $L_2 = 0.5$, $L_3 = 1.39$, $R_1 = 0.35$, $R_2 = 0.15$, $H_1 = 0.5$, $H_2 = 0.2$. As shown in Figure 2, the eccentric feeding is adopted to obtain the left-hand circular polarization. The rectangular patch is fed at the diagonal by a vertical probe to excite two orthogonal modes for circularly polarized radiation.

The simulated voltage standing wave ratio (VSWR) and axial ratio (AR) are plotted in Fig. 3. It is observed that the impedance bandwidth with VSWR < 2 is 10.8% (28.3-31.6 GHz) and the AR bandwidth with AR $<$ 3dB is approximately 5.0% (29.4-30.9GHz). The antenna element is left-hand circular polarization (LHCP) and has a peak simulated gain of 6.23 dBi at 30 GHz.

Based on the single antenna element above, a 52-element antenna array is constructed, as shown in Fig. 4. The 52 antenna elements are arranged into a rectangular array, which occupies a total area of 46 mm×44 mm. As shown in Fig. 4, sequential rotation feeding scheme is adopt in the 2 × 2 sub-array.

In order to improve the circularly polarized performance, the four-antenna element are rotated with respect to each other and excited with 90° phase difference increments, and the phase shifts are introduced by the phase shifters in the Tx modules. The distance between the elements is 5 mm, which is a half of the wavelength in free space at 30 GHz. Figure 5(a) presents the simulated radiation patterns of the antenna array at 30 GHz. It is observed that the antenna array

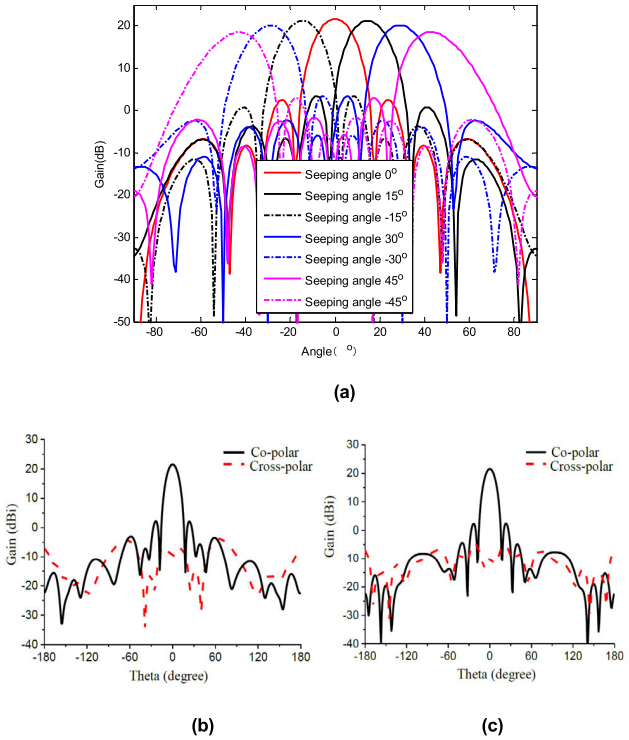

FIGURE 5. Simulated radiation patterns of the antenna array at 30 GHz. (a) Beam steering (b) *xoz*-plane (c) *yoz*-plane.

has a peak gain of 21.6 dB and the side-lobe levels (SLL) are about -15 dB in the ±45° sweeping scope. The patterns in *xoz* and *yoz* planes are shown in Fig. 5(b) and Fig. 5(c), respectively. It is observed that the antenna array has a peak gain of 21.5 dBi and the cross-polarization levels are below -20 dBc. Besides, the side-lobe levels (SLL) in *xoz*-plane and *yoz*-plane are about -18.1 and -18.3 dBc, respectively.

Figure 6(a) shows the block diagram of the active antenna array. The input RF signal is divided by a 1:16 stripline feeding network. The feeding network with a thickness of 4 LTCC layers contains four-stage Wilkinson dividers illustrated in Fig. 6(b). Simulated results show that the input VSWR of the feeding network is below 1.5 over the frequency range from 28 to 31.8 GHz, the phase imbalance of output ports is less than 1.6 degree, and the power imbalance is about 0.3 dB. Then, the output signals of the dividers are shifted in phase and amplified by power amplifiers in the Tx modules. The active Tx modules are composed of 16 sets of transmitter chips. As shown in Fig. 6 (b), each of the transmitter chipsets at the four corners of the board consist of a 6-bit digital phase-shifter and a power amplifier, and each of the other 12 chipsets consist of four-phase shifter and four power amplifiers. A 1:4 power divider and four 5-bit digital phase-shifters are incorporated in the multi-channel phase shifter. Finally, the output RF signals are fed to each element of the antenna array. Compared with conventional RF transmitter chip sets with a phase shifter and a power amplifier for each antenna element, the proposed RF front end has less integrated chips and occupies a smaller area.

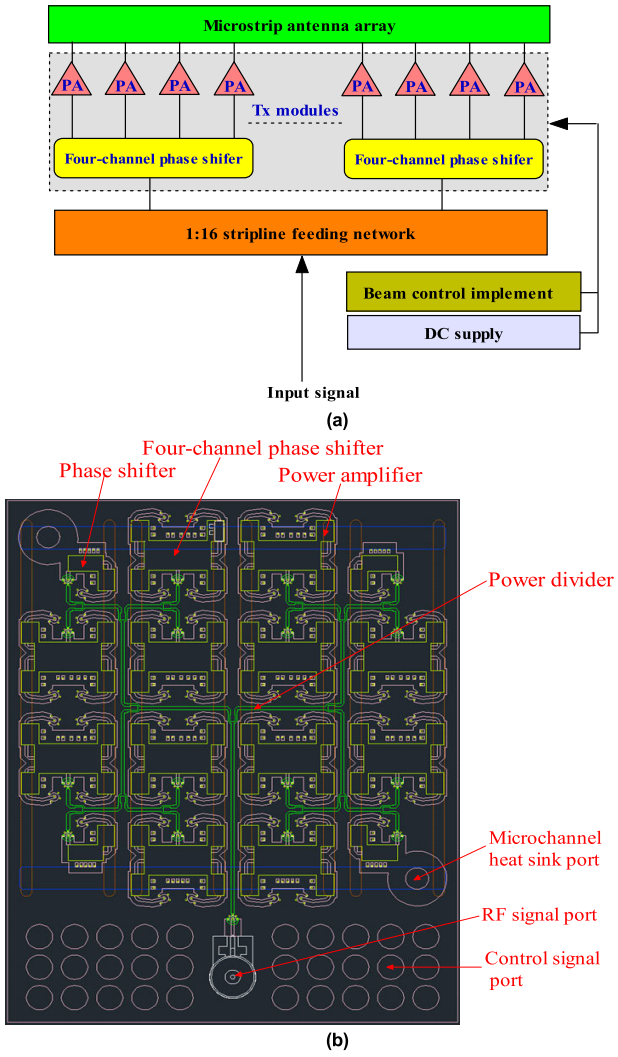

FIGURE 6. Structure of the active antenna (a) Block diagram of the active antenna. (b) Structure of the power divider and layout of the Tx modules.

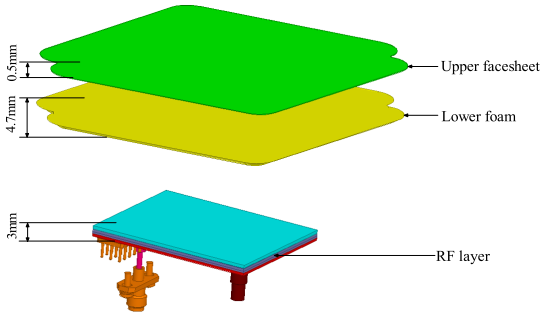

FIGURE 7. Structural configuration and dimensions of the superstrates in front of the RF layer.

Subsequently, the next step is to determine the super-strates composed of the upper face-sheet and lower foam depicted in Fig. 7. The thickness of the super-strates locating above the antenna array not only contributes to the structural stiffness and strength, but also influences the

TABLE 1. Electrical properties of the materials.

Name	MATERIAL NAME	Electrical properties
Facesheet	Glass/epoxy	$\varepsilon_r = 4, \tan\delta = 0.02$
Foam	PMI foam	$\varepsilon_r = 1.1, \tan\delta = 0.005$
RF layer	Ferro A6M	$\varepsilon_r = 5.9, \tan\delta = 0.002$

TABLE 2. Mechanical properties of the materials.

	Glass/epoxy	Foam	Aluminum	Foam
Elastic modulus (MPa)	40000	160	71000	92000
Poisson ratio	0.26	0.4	0.33	0.2
Density Kg/cm^3	1800	110	2700	2450

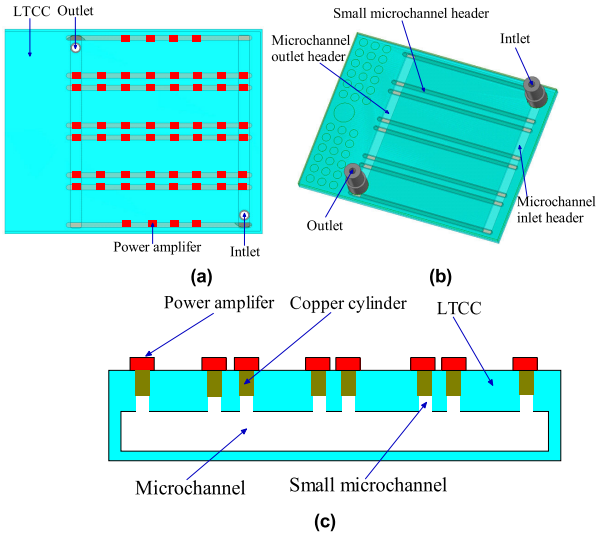

FIGURE 8. Structural configuration of micro-channel heat sinks. (a) Top view (b) Back view(c) Cross section view.

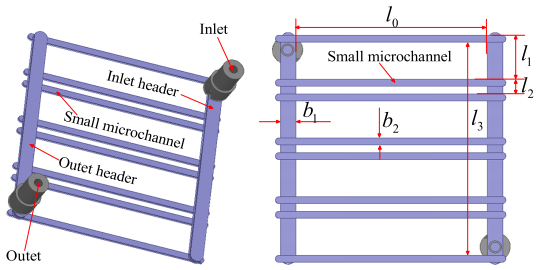

FIGURE 9. Geometry of micro-channel heat sinks.

electromagnetic performance. In order to meet the mechanical and electrical requirements simultaneously, the electromechanical co-design method is developed to design the super-strates.Tables 1 and 2 give the electrical and mechanical properties of the materials used in the antenna structure.

The coarse thicknesses of the facesheet and foam are optimized by the electromechanical co-design method in [34]. The coarse thickness can provide an optimal structural stiffness and strength. However, it cannot guarantee an optimal design for the electromagnetic performance of the antenna array with the super-strates. In the last step, the coarse dimensions were applied to develop a full-wave electromagnetic model using the commercial simulation software HFSS from ANSYS. The thicknesses of the face-sheet and foam were further optimized and the final dimensions of the super-strates are determined as indicated in Fig. 7.

C. DESIGN OF MICRO-CHANNEL HEAT SINK

As mentioned above, high-power amplifiers are adopted in the Tx modules to enhance the signal power level. However, each amplifier is a heat source, which could influence the electrical performance of the active antenna array. In this work, a micro-channel heat sink is designed to cool the RF front end. Figure 8 shows the structural configuration of the micro-channel heat sink which consists of a micro-channel inlet header and a micro-channel outlet header, eight small micro-channels, an inlet and an outlet.

The micro-channel heat sink is fabricated based on the LTCC technology, and it is convenient to integrate the micro-channel heat sinks into the RF layer. However, because of a low heat transfer coefficient of the LTCC, it is slow to cool the RF layer. Therefore, under each high-power amplifier, a copper cylinder is utilized to connect the high-power amplifier (heat source) with the small micro-channel. Figure 8(c) shows the cross section of a micro-channel in the RF layer. The diameter and height of the copper cylinder are 1 and 1.2 mm, respectively. The coolant from the inlet flows into the micro-channel inlet header, and then is shunted into eight small micro-channels. The heat passes through the copper cylinder to the coolant, and then the coolant from the small micro-channels meets at the outlet header and flows away from the outlet. Utilizing the coolant movements, the heat is dissipated from the RF layer.

With the same coolant, the greater the flow rate of the coolant, the better the heat dissipation. Moreover, the more uniform the flow rate of the coolant in different micro-channels, the more uniform the temperature distribution in RF layer. The non-uniformity of the temperature distribution in the RF layer can lead to an inconsistent amplitude and phase variations of radiating element excitations which deteriorate the electrical performance of the active antenna array. In order to obtain a uniform temperature distribution, two schemes are designed, analyzed and compared in the following.

Figure 9 shows the geometry structure of micro-channel heat sinks. The cross section of the micro-channel heat sink is rectangle. The length, width and height of the inlet header and outlet header are 40 mm, 2.2 mm and 0.8 mm, respectively. The length, width and height of the small micro-channel are 36 mm, 1mm and 0.6 mm, respectively. The detailed

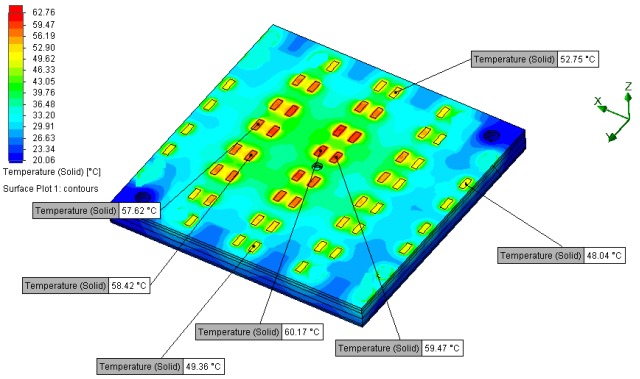

FIGURE 10. Temperature field distribution.

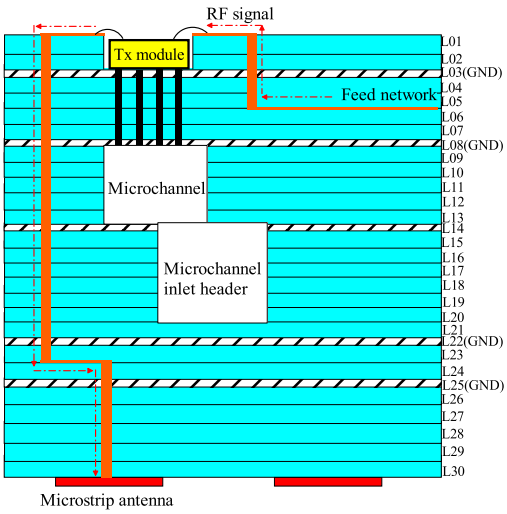

FIGURE 11. Cross section of the Ferro A6M tapes layout in the RF layer.

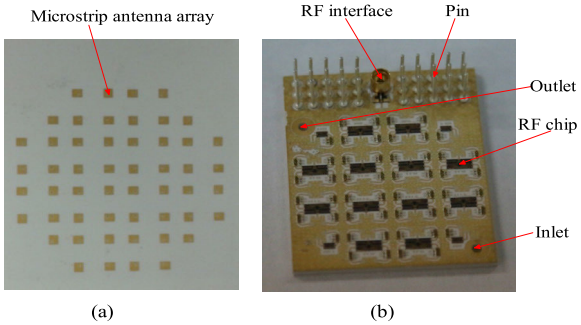

FIGURE 12. RF layer specimen. (a) Front view. (b) Back view.

dimensions of the optimized parameters in Fig. 10 are as follows (unit: mm): $l_0 = 36$, $l_1 = 8$, $l_2 = 3$, $l_3 = 40$, $b_1 = 2.2$, $b_2 = 1$. Numerical simulations are conducted to obtain the temperature fields of two schemes for the micro-channel heat sinks. Tables III and IV give the material properties and boundary conditions required by the simulation software ANSYS CFX. Figure 10 presents the temperature field distributions of structurally integrated active antenna. It can be observed from Fig. 10 that the temperature scope is from 48.04°C to 60.17°C.

Table 5 gives the statistical results of the temperature distributions on the surface of the RF layer. It also provides the standard deviation of the temperature and maximum temperature difference, which quantitatively evaluate the uniformity of the temperature distribution with and without heat sinks. The small deviation of the temperature and maximum temperature difference will cause smaller amplitude and phase variations of the radiating element excitations, which can provide a stable antenna electrical performance. From Tab. 5, it is obviously concluded that the scheme with heat sinks can provide a more uniform temperature distribution than that without the heat sinks. The impact from the heat sinks on the performance of the array system is discussed in Sec. V.

TABLE 3. Material properties of microchannel heat sink.

Name	Thermal conductivity (W/m.k)	Density (Kg/m^3)	Specific heat capacity (J/Kg.K)
Deionized water	0.613	997	4179
LTCC	2	2450	849
Copper	401	8933	385

III. FABRICATION

This section presents the fabrication of the structurally integrated phased array prototype. In the first step, according to the design above, the LTCC technology was exploited to fabricate the RF layer. In this work, the RF layer is made of 25 layers Ferro A6M tapes and 5 layers copper tapes (GND). Figure 11 presents a cross section of the 30 layers tapes layout. The micro-channel heat sinks are laminated with 12 layer tapes. The methods based on sacrificial volume materials (SVM) are applied to fabricate the micro-channels, and the SVM materials (i.e. carbon-black paste) are applied to fill in the micro-channels before the green tapes were sintered. The LTCC process begins with punching the via holes in the green ceramic tapes. Then, the via holes are metallized followed by the conductor patterning on each tape layer separately. Conductors are patterned using screen-printing techniques. After the tape sheets are aligned and laminated, the ceramic sheets are co-fired at the 850°, and then the SVM evaporates in a pressurized environment of the high temperature, which shapes the resulting micro-channels. Finally, the transmitter chips are welded to the surface of the RF layer. The wire-bonding technique is applied to realize the interconnection between the Tx modules and the feeding network. Figures 12(a) and (b) show the front view and back view of the RF layer specimen, respectively, and the length, width and thickness of the specimen are 46 mm, 44 mm and 2.8 mm, respectively.

Then, the fabricated control and signal process layer is shown in Fig. 13. First, the beam control circuit is fabricated by using the PCB manufacturing technology. Then, the pin connections are applied to realize the interconnection

TABLE 4. Boundary conditions for numerical simulations.

Coolant	Deionized water
Inlet flow rate	500 ml/min
Temperature of the inlet fluid	293K
Environment temperature	295K
Heat flux	56.25W/cm2

TABLE 5. Statistical results of the temperature distribution.

Temperature	Highest temperature (^{0}C)	Standard deviation (^{0}C)	Maximum temperature difference (℃)
With heat sinks	60.17	2.56	10.2
Without heat sinks	137.26	22.6	41

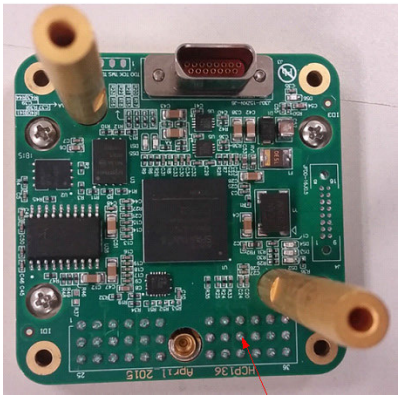

FIGURE 13. Control and signal process layer.

between the beam control circuit and the DC power. The interconnections are conducted to form an initial assembly of the active antenna array without the package layer. The connections of different layers are shown in Fig. 14. Figure 14(a) shows the interconnection between the RF layer and the control and signal process layer, and two groups of pins (36 pins in all) are applied to connect the RF chips and the beam control circuit. Figure 14(b) shows the interface between the RF layer and external devices. The control and signal process layer is removed from the drawing, to allow a deeper insight into the structure. The inlet and the outlet which connect the RF layer and external devices, go through the control and signal process layer. The wire crosses the DC power, and connects the beam control circuit and an external computer terminal. Finally, the package layer is fabricated, and the antenna and the package layer are integrated to form the final antenna prototype by using the composite technology. In this step, the package layer consists of the encapsulate shell and the super-strates is made of aluminum to improve the structural stiffness and strength. The super-strate consists of the lower foam and the radome which is composited by the upper facesheet. After the package layer is fabricated, the active antenna array in the step 3 is put inside the encapsulate shell as shown in 14.

The encapsulate shell is made of aluminum to improve the structural stiffness and strength. The super-strate consists

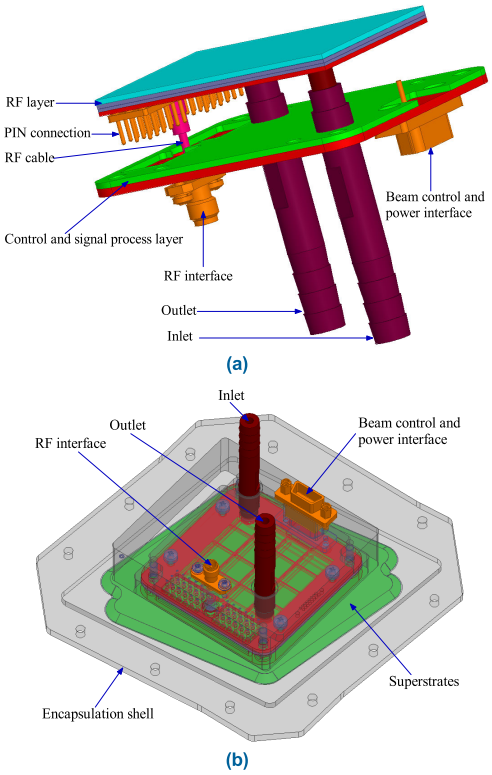

FIGURE 14. Connections of different layers. (a) Interconnections between the RF layer and the control and signal process layer. (b) Interconnections between the RF layer and the package layer.

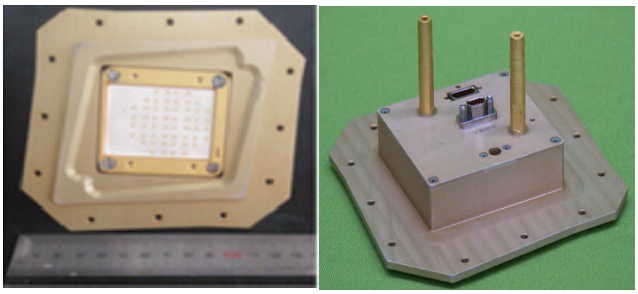

FIGURE 15. Structurally integrated phased array prototype. (a) Front view. (b) Back view.

of the lower foam and the radome which is composited by the upper facesheet. After the package layer was fabricated, the active antenna array in the step 3 was put inside the encapsulate shell as shown in Fig.15(a). Subsequently, the radome, the lower foam and the active antenna were bonded by using the composite technology. Each component is bonded on the top or bottom of another one in designed sequence. Figure 15 shows the fabricated antenna prototype.

IV. EXPERIMENT RESULTS

In this section, experiments are carried out to validate the electromagnetic performance. To demonstrate the electromagnetic performance, the radiation characteristics of the

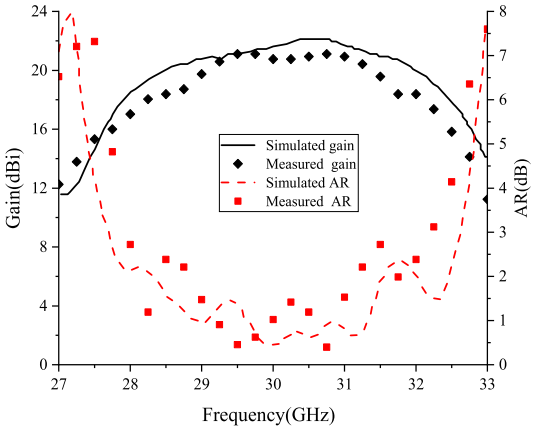

FIGURE 16. Measured and simulated gain and AR at the different frequency.

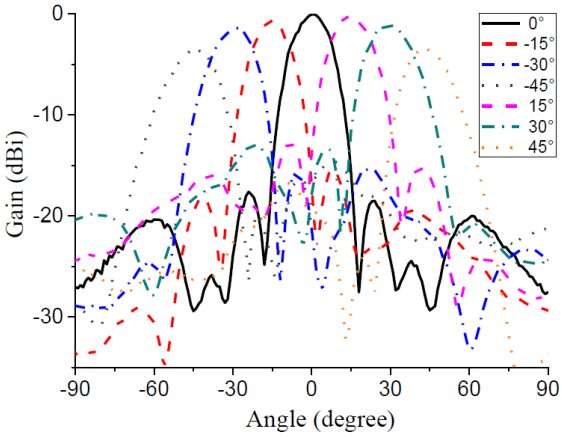

FIGURE 17. Measured normalized scanning patterns of the structurally integrated phased array prototype at 30 GHz.

fabricated antenna prototype were measured in an anechoic chamber. Figure 16 shows the measured and simulated gain and AR against frequency of the antenna prototype. It is observed that the measured 3-dB gain bandwidth ranges from about 28.5 GHz to 32 GHz with a peak gain of 21.0 dBi, while the 3-dB AR bandwidth is from around 28 GHz to 32.2 GHz. The measured and simulated results are overall in good agreement, and the discrepancy is due to the fabrication tolerance and measurement errors.

Figure 17 plots the scanning patterns in the azimuth plane at 30 GHz. The measured scanning range is from $-45°$ to $45°$, and the measured beam direction exhibits slight difference from the expected scanning angle ($-45°$ to $+45°$). This difference may be due to the imperfections of the measurement system such as the phase error caused by the cables, adapters and alignment issues. The gain fluctuations within the scanning range are smaller than 3.5 dB, and the side-lobe levels are better than -12 dB. Moreover, it is found that the gain fluctuation is less than 1.5 dB when the scanning angle ranges from $-30°$ to $+30°$. When the scanning angle is beyond $\pm 30°$, the gain drops by more than 3dB. This could be

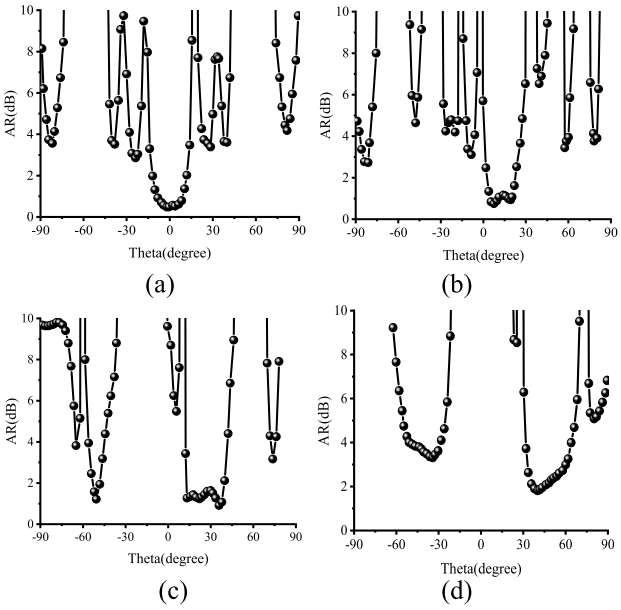

FIGURE 18. Measured axial ratio with beam scanned to different angles at 30GHz, (a) $\theta = 0°$, (b) $\theta = 15°$, (c) $\theta = 30°$, (d) $\theta = 45°$ ($\varphi = 0°$ plane).

attributed to the roll-off of the antenna element patterns that get flattened due to the mutual coupling between the radiating elements.

The AR performance of array is also measured. As shown in Fig. 18, the ARs are below 3 dB within the 3dB beam width of the main beam, when the main beam is steered to 0, 15, 30 and 45°.

V. DISCUSSION

The mechanical structures and the thermal effects do affect the performance of the array. There are two mechanical structures that affect array performance. One is the radome and the other is the radiator. The other one is the heat sinks. The function of the radome is to protect the antenna front. However, after the radome is introduced, the matching between the array and free space is destroyed, so that the radiation efficiency of the array will be reduced, and eventually the radiation efficiency of the array will be reduced. Therefore, there is a trade-off between radome design and radiation efficiency. The material of the radome should have low dielectric constant to reduce the impact on the matching of the antenna to free space. At the same time, the radome should be low lossy to reduce dielectric loss. In our work, the material of the upper sheet of the radome is glass with $\varepsilon_r = 4$, $\tan\delta = 0.02$, while the lower sheet of the radome is foam with $\varepsilon_r = 1.1$, $\tan\delta = 0.005$. Figure 19 shows the change in gain with and without radome. It can be seen from Fig. 19 that with a radome, the array gain will drop, however, above 30 GHz, the gain decreases less than 2 dBi.

The heat sink structure does not directly affect the electrical performance of the antenna. The micro-channel heat sink is designed to cool the RF front end. Without the heat sink, as shown in Tab. 5, the highest temperature in the RF layer

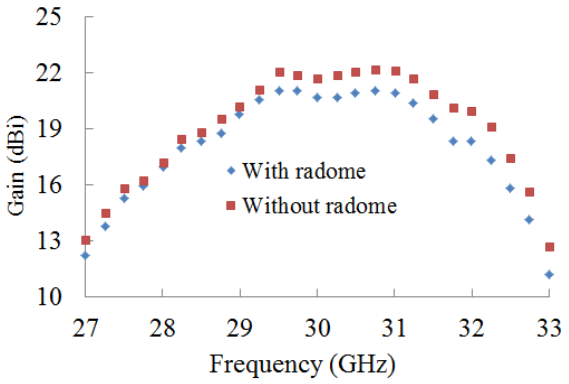

FIGURE 19. Changes of the Gain with and without radome.

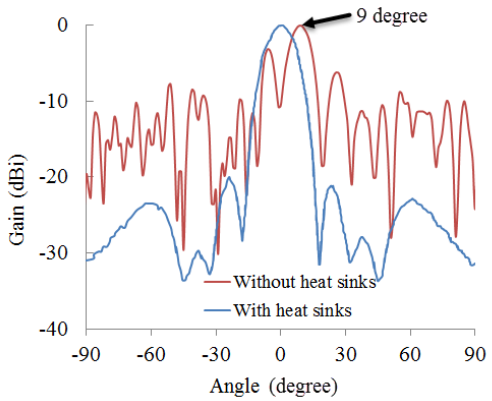

FIGURE 20. Patterns of the array with and without heat sinks at 30 GHz (in-phase feeding).

reaches 137 °C. At such high temperature, solid-state devices at the RF layer cannot work properly. When the phased array works for a long time without heat dissipation structure, the amplitude and phase consistency of the RF channel deteriorate, and part of RF channels are even damaged. Therefore, the heat sink will indirectly affect the performance of the array. Figure 20 shows the radiation pattern of the array with and without a heat sink. It can be observed that, without heat sinks, the side lobe of the pattern is raised, and the main lobe pattern deviates under the condition of in-phase feeding. The array is no longer working properly. In summary, the heat dissipation structure is particularly important for arrays. Owing to the heat sinks, the temperature in the RF layer is controlled within the operating temperature of the solid-state device.

VI. CONCLUSION

This work presents the design, fabrication and testing of a Ka-band structurally integrated phased array. The electromechanical co-design methods are applied to design the package layer, the control and signal process layer and an RF layer. Thermal analysis of the RF layer is also carried out. The effects of mechanical structure and thermal effects on the performance of the antenna array are analyzed. The measurement results demonstrate the feasibility of the structurally integrated active antenna for airborne wireless communications.

ACKNOWLEDGMENT

The authors would like to thank Ming Yao, Yi Li, Jian Zhang, Qing Zhao, and Shun-Ping Yang for their contributions in the design of the antenna prototype.

REFERENCES

[1] B. Sadhu *et al.*, "A 28-GHz 32-element TRX phased-array IC with concurrent dual-polarized operation and orthogonal phase and gain control for 5G communications," *IEEE J. Solid-State Circuits*, vol. 52, no. 12, pp. 3373–3391, Dec. 2017.

[2] S. Shahramian, M. J. Holyoak, and Y. Baeyens, "A 16-element W-band phased-array transceiver chipset with flip-chip PCB integrated antennas for multi-gigabit wireless data links," *IEEE Trans. Microw. Theory Techn.*, vol. 66, no. 7, pp. 3389–3402, Jul. 2018.

[3] K. Kibaroglu, M. Sayginer, and G. M. Rebeiz, "A low-cost scalable 32-element 28-GHz phased array transceiver for 5G communication links based on a 2 × 2 beamformer flip-chip unit cell," *IEEE J. Solid-State Circuits*, vol. 53, no. 5, pp. 1260–1274, May 2018.

[4] Z. Cao, Q. Ma, A. B. Smolders, Y. Jiao, M. J. Wale, C. W. Oh, H. Wu, and A. M. J. Koonen, "Advanced integration techniques on broadband millimeter-wave beam steering for 5G wireless networks and beyond," *IEEE J. Quantum Electron.*, vol. 52, no. 1, pp. 1–20, Jan. 2016.

[5] F. Tabarani, L. Boccia, T. Purtova, A. Shamsafar, H. Schumacher, and G. Amendola, "0.25-μm BiCMOS system-on-chip for K-/Ka-band satellite communication transmit–receive active phased arrays," *IEEE Trans. Microw. Theory Techn.*, vol. 66, no. 5, pp. 2325–2339, May 2018.

[6] F. Foglia Manzillo, M. Ettorre, M. S. Lahti, K. T. Kautio, D. Lelaidier, E. Seguenot, and R. Sauleau, "A multilayer LTCC solution for integrating 5G access point antenna modules," *IEEE Trans. Microw. Theory Techn.*, vol. 64, no. 7, pp. 2272–2283, Jul. 2016.

[7] H. Schippers, J. Verpoorte, A. Hulzinga, C. Roeloffzen, and R. Baggen, "Towards structural integration of airborne Ku-band SatCom antenna," in *Proc. 7th Eur. Conf. Antennas Propag. (EuCAP)*, Apr. 2013, pp. 2963–2967.

[8] M. Urcia and D. Banks, "Structurally integrated phased arrays," in *Proc. IEEE Aerosp. Conf. (AERO)*, Big Sky, MT, USA, Mar. 2011, pp. 1–8.

[9] J. Zhou, J. Huang, L. Song, D. Zhang, and Y. Ma, "Electromechanical co-design and experiment of structurally integrated antenna," *Smart Mater. Struct.*, vol. 24, no. 3, Mar. 2015, Art. no. 037004.

[10] S. Shahramian, M. Holyoak, A. Singh, B. J. Farahani, and Y. Baeyens, "A fully integrated scalable W-band phased-array module with integrated antennas, self-alignment and self-test," in *IEEE Int. Solid-State Circuits Conf. (ISSCC) Dig. Tech. Papers*, Feb. 2018, pp. 74–76.

[11] B. Curran, J. Reyes, C. Tschoban, J. Hofer, A. Grams, F. Wust, M. Hutter, J. Leib, M. Martinez-Vazquez, R. Baggen, I. Ndip, and K.-D. Lang, "Development and validation of a chip integration concept for multi-die GaAs front ends for phased arrays up to 60 GHz," *IEEE Trans. Compon., Packag., Manuf. Technol.*, vol. 8, no. 7, pp. 1231–1240, Jul. 2018.

[12] Y. P. Zhang and D. Liu, "Antenna-on-chip and antenna-in-package solutions to highly integrated millimeter-wave devices for wireless communications," *IEEE Trans. Antennas Propag.*, vol. 57, no. 10, pp. 2830–2841, Oct. 2009.

[13] Y. P. Zhang, M. Sun, K. M. Chua, L. L. Wai, and D. Liu, "Antenna-in-package design for wirebond interconnection to highly integrated 60-GHz radios," *IEEE Trans. Antennas Propag.*, vol. 57, no. 10, pp. 2842–2852, Oct. 2009.

[14] D. Liu, X. Gu, C. W. Baks, and A. Valdes-Garcia, "Antenna-in-package design considerations for ka-band 5G communication applications," *IEEE Trans. Antennas Propag.*, vol. 65, no. 12, pp. 6372–6379, Dec. 2017.

[15] C.-C. Liu and R. G. Rojas, "V-band integrated on-chip antenna implemented with a partially reflective surface in standard 0.13-μm BiCMOS technology," *IEEE Trans. Antennas Propag.*, vol. 64, no. 12, pp. 5102–5109, Dec. 2016.

[16] J. C. Johnstone, B. M. Frank, and Y. M. M. Antar, "Coupled loops for high-frequency chip-to-antenna interconnection at 24 GHz," *IEEE Trans. Microw. Theory Techn.*, vol. 62, no. 5, pp. 1203–1211, May 2014.

[17] U. Ullah, N. Mahyuddin, Z. Arifin, M. Z. Abdullah, and A. Marzuki, "Antenna in LTCC technologies: A review and the current state of the art," *IEEE Antennas Propag. Mag.*, vol. 57, no. 2, pp. 241–260, Apr. 2015.
[18] M. Sun, Y. P. Zhang, K. M. Chua, L. L. Wai, D. Liu, and B. P. Gaucher, "Integration of Yagi antenna in LTCC package for differential 60-GHz radio," *IEEE Trans. Antennas Propag.*, vol. 56, no. 8, pp. 2780–2783, Aug. 2008.
[19] D. G. Kam, D. Liu, A. Natarajan, S. Reynolds, H.-C. Chen, and B. A. Floyd, "LTCC packages with embedded phased-array antennas for 60 GHz communications," *IEEE Microw. Wireless Compon. Lett.*, vol. 21, no. 3, pp. 142–144, Mar. 2011.
[20] D. Liu, J. A. G. Akkermans, H.-C. Chen, and B. Floyd, "Packages with integrated 60-GHz aperture-coupled patch antennas," *IEEE Trans. Antennas Propag.*, vol. 59, no. 10, pp. 3607–3616, Oct. 2011.
[21] W. Zhang, Y. P. Zhang, M. Sun, C. Luxey, D. Titz, and F. Ferrero, "A 60-GHz circularly-polarized array Antenna-in-Package in LTCC technology," *IEEE Trans. Antennas Propag.*, vol. 61, no. 12, pp. 6228–6232, Dec. 2013.
[22] W. Hong, K.-H. Baek, Y. Lee, Y. Kim, and S.-T. Ko, "Study and prototyping of practically large-scale mmWave antenna systems for 5G cellular devices," *IEEE Commun. Mag.*, vol. 52, no. 9, pp. 63–69, Sep. 2014.
[23] B. Zhang, D. Titz, F. Ferrero, C. Luxey, and Y. Ping Zhang, "Integration of quadruple linearly-polarized microstrip grid array antennas for 60-GHz antenna-in-package applications," *IEEE Trans. Compon., Packag., Manuf. Technol.*, vol. 3, no. 8, pp. 1293–1300, Aug. 2013.
[24] S. Beer, H. Gulan, C. Rusch, and T. Zwick, "Integrated 122-GHz antenna on a flexible polyimide substrate with flip chip interconnect," *IEEE Trans. Antennas Propag.*, vol. 61, no. 4, pp. 1564–1572, Apr. 2013.
[25] B. Zhang, H. Gulan, T. Zwick, Y. Li, U. Oderfalt, F. Carlsson, and H. Zirath, "Integration of a 140 GHz packaged LTCC grid array antenna with an InP detector," *IEEE Trans. Compon., Packag., Manuf. Technol.*, vol. 5, no. 8, pp. 1060–1068, Aug. 2015.
[26] D. G. Kam, D. Liu, A. Natarajan, S. K. Reynolds, and B. A. Floyd, "Organic packages with embedded phased-array antennas for 60-GHz wireless chipsets," *IEEE Trans. Compon., Packag., Manuf. Technol.*, vol. 1, no. 11, pp. 1806–1814, Nov. 2011.
[27] J.-C.-S. Chieh, B. Pham, A.-V. Pham, G. Kannell, and A. Pidwerbetsky, "Millimeter-wave dual-polarized high-isolation antennas and arrays on organic substrates," *IEEE Trans. Antennas Propag.*, vol. 61, no. 12, pp. 5948–5957, Dec. 2013.
[28] W. T. Khan, A. L. V. Lopez, A. C. Ulusoy, and J. Papapolymerou, "Packaging a *W*-band integrated module with an optimized flip-chip interconnect on an organic substrate," *IEEE Trans. Microw. Theory Techn.*, vol. 62, no. 1, pp. 64–72, Jan. 2014.
[29] B. Zhang, C. Karnfelt, H. Gulan, T. Zwick, and H. Zirath, "A *D*-band packaged antenna on organic substrate with high fault tolerance for mass production," *IEEE Trans. Compon., Packag., Manuf. Technol.*, vol. 6, no. 3, pp. 359–365, Mar. 2016.
[30] Y. Zhou, Y. Bayram, F. Du, L. Dai, and J. L. Volakis, "Polymer-carbon nanotube sheets for conformal load bearing antennas," *IEEE Trans. Antennas Propag.*, vol. 58, no. 7, pp. 2169–2175, Jul. 2010.
[31] S. E. Morris, Y. Bayram, L. Zhang, Z. Wang, M. Shtein, and J. L. Volakis, "High-strength, metalized fibers for conformal load bearing antenna applications," *IEEE Trans. Antennas Propag.*, vol. 59, no. 9, pp. 3458–3462, Sep. 2011.
[32] N. A. Bishop, J. Miller, D. Zeppettella, W. Baron, J. Tuss, and M. Ali, "A broadband high-gain bi-layer LPDA for UHF conformal load-bearing antenna structures (CLASs) applications," *IEEE Trans. Antennas Propag.*, vol. 63, no. 5, pp. 2359–2364, May 2015.
[33] S. H. Son, S. Y. Eom, and W. Hwang, "Development of a smart-skin phased array system with a honeycomb sandwich microstrip antenna," *Smart Mater. Struct.*, vol. 17, no. 3, Jun. 2008, Art. no. 035012.
[34] L. Yao, X. Wang, F. Xu, D. Zhao, M. Jiang, and Y. Qiu, "Fabrication and impact performance of three-dimensionally integrated microstrip antennas with microstrip and coaxial feeding," *Smart Mater. Struct.*, vol. 18, no. 9, Sep. 2009, Art. no. 095034.
[35] C. You, D. Kim, S. Cho, and W. Hwang, "Impact behavior of composite antenna array that is conformed around cylindrical bodies," *Compos. Sci. Technol.*, vol. 70, no. 4, pp. 627–632, Apr. 2010.
[36] A. B. Smolders and U. Johannsen, "Axial ratio enhancement for circularly-polarized millimeter-wave phased-arrays using a sequential rotation technique," *IEEE Trans. Antennas Propag.*, vol. 59, no. 9, pp. 3465–3469, Sep. 2011.
[37] B. Zhang, Y. P. Zhang, D. Titz, F. Ferrero, and C. Luxey, "A circularly-polarized array antenna using linearly-polarized sub grid arrays for highly-integrated 60-GHz radio," *IEEE Trans. Antennas Propag.*, vol. 61, no. 1, pp. 436–439, Jan. 2013.
[38] H. Sun, Y.-X. Guo, and Z. Wang, "60-GHz circularly polarized U-slot patch antenna array on LTCC," *IEEE Trans. Antennas Propag.*, vol. 61, no. 1, pp. 430–435, Jan. 2013.
[39] M. Sun, Y.-Q. Zhang, Y.-X. Guo, M. F. Karim, O. L. Chuen, and M. S. Leong, "Integration of circular polarized array and LNA in LTCC as a 60-GHz active receiving antenna," *IEEE Trans. Antennas Propag.*, vol. 59, no. 8, pp. 3083–3089, Aug. 2011.
[40] K. Malecha and L. J. Golonka, "Microchannel fabrication process in LTCC ceramics," *Microelectron. Rel.*, vol. 48, no. 6, pp. 866–871, Jun. 2008.

QING-QIANG HE received the M.S. degree in electromagnetic and microwave technology and the Ph.D. degree in radio physics from the University of Electronic Science and Technology of China, in 2005 and 2008, respectively. He is currently a Senior Engineer with the Southwest China Institute of Electronic Technology, Chengdu, China. He has published more than 70 articles in journals and conference proceedings. He owns 13 patents issued and four patents pending. His research interests include phased array antennas and antenna theory and techniques.

SHUAI DING received the Ph.D. degree in radio physics from the University of Electronic Science and Technology of China (UESTC), Chengdu, in 2013. From 2013 to 2014, he was a Postdoctoral Associate with the École Polytechnique de Montréal, QC, Canada. In 2015, he joined UESTC, where he is currently an Associate Professor. He has authored or coauthored over 80 publications in refereed journals and international conferences/symposia. His current research interests include time-reversed electromagnetics and its applications to communication and energy transmission, phased array, analog signal processing, and microwave circuits. He has served as a TPC Member for various conferences and a Reviewer for several peer-reviewed periodicals and international conferences/symposia.

CHEN XING received the M.S. degree from the University of Electronic Science and Technology of China, in 2014. He is currently an Engineer with the Southwest China Institute of Electronic Technology, Chengdu, China. His research interests include phased array antennas and microwave networks.

JUN-QUAN CHEN received the Ph.D. degree in radio physics from the College of Electronic and Information Engineering, Sichuan University, in 2013. He is currently a Senior Engineer with the Southwest China Institute of Electronic Technology, Chengdu, China. His research interests include phased array antennas and antenna theory and techniques.

GUO-QING YANG received the M.S. degree in electromagnetic and microwave technology from the University of Electronic Science and Technology of China, in 2012. He is currently an Engineer with the Southwest China Institute of Electronic Technology, Chengdu, China. His research interests include phased array antennas and microwave components techniques.

BING-ZHONG WANG (Senior Member, IEEE) received the Ph.D. degree in electronic engineering from the University of Electronic Science and Technology of China (UESTC), Chengdu, in 1988.

He joined UESTC, in 1984, where he is currently a Professor. He has been a Visiting Scholar with the University of Wisconsin-Milwaukee, WI, USA, a Research Fellow with the City University of Hong Kong, Hong Kong, and a Visiting Professor with the Electromagnetic Communication Laboratory, Pennsylvania State University, University Park, PA, USA. His current research interests include computational electromagnetics, antenna theory and techniques, and time-reversed electromagnetics.